A far-infrared radiative closure study in the Arctic: Application to water vapor

J. S. Delamere,[1] S. A. Clough,[2] V. H. Payne,[1] E. J. Mlawer,[1] D. D. Turner,[3] and R. R. Gamache[4]

Received 12 August 2009; revised 16 February 2010; accepted 7 April 2010; published 8 September 2010.

[1] Far-infrared ($\lambda > 15.0$ μm) (far-IR) radiative processes provide a large fraction of Earth's outgoing longwave radiation and influence upper tropospheric vertical motion. Water vapor, because of its abundance and strong absorption properties over an extended spectral range, is the primary source of these radiative processes. Historically, the lack of spectrally resolved radiometric instruments and the opacity of the lower atmosphere have precluded extensive studies of far-IR water vapor absorption properties. The U.S. Department of Energy Atmospheric Radiation Measurement (ARM) program has organized a series of field experiments, the Radiative Heating in Underexplored Bands Campaigns (RHUBC), to address this deficiency. The first phase of RHUBC took place in 2007 at the ARM North Slope of Alaska Climate Research Facility. Measurements taken before and during this campaign have provided the basis for a clear-sky radiative closure study aimed at reducing key uncertainties associated with far-IR radiative transfer models. Extended-range Atmospheric Emitted Radiance Interferometer infrared radiance observations taken in clear sky conditions were compared against calculations from the Line-By-Line Radiative Transfer Model. The water vapor column amounts used in these calculations were retrieved from 183 GHz radiometer measurements. The uncertainty in these integrated water vapor retrievals is approximately 2%, a notable improvement over past studies. This far-IR radiative closure study resulted in an improvement to the Mlawer-Tobin Clough-Kneiyzs-Davies (MT_CKD) water vapor foreign continuum model and updates to numerous, far-IR water vapor line parameters from their values in the circa 2006 version of the HITRAN molecular line parameter database.

Citation: Delamere, J. S., S. A. Clough, V. H. Payne, E. J. Mlawer, D. D. Turner, and R. R. Gamache (2010), A far-infrared radiative closure study in the Arctic: Application to water vapor, *J. Geophys. Res.*, *115*, D17106, doi:10.1029/2009JD012968.

1. Introduction

[2] The far-infrared (far-IR) portion of the electromagnetic spectrum ($\nu < 667$ cm^{-1}, $\lambda > 15.0$ μm) has an important role in determining Earth's energy budget [e.g., *Clough et al.*, 1992; *Harries et al.*, 2008]. Up to 45% of the total outgoing longwave radiation to space, as well as the majority of mid to upper tropospheric cooling, occurs in this spectral region. The far-IR also shows the greatest sensitivity to perturbations in upper tropospheric humidity [*Sinha and Harries*, 1995]. Because of its abundance, strong rotation band absorption properties, and the extended spectral domain over which it is active, water vapor is a key source of far-IR atmospheric radiative processes. Water vapor absorption is often modeled as a combination of two components: a contribution from near spectral line centers, described by the Voigt line shape, and the water vapor continuum, a slowly varying function derived to provide agreement with measurements [e.g., *Clough et al.*, 1989]. Both components are required to accurately model radiative processes in the Earth's atmosphere.

[3] Historically, the lack of spectrally resolved radiometric instruments and the opacity of the lower atmosphere have precluded extensive studies of far-IR water vapor absorption. For a typical moist atmosphere, the spectrum is opaque below 530 cm^{-1}, but transmission significantly increases in the microwindows (regions between absorption line centers) as the precipitable water vapor (PWV) decreases. Figure 1 shows the calculated downwelling atmospheric radiance received at the surface and the atmospheric transmittance for three atmospheric profiles: the U.S. Standard Atmosphere (1.43 cm PWV, green), a PWV-scaled Subarctic Winter Atmosphere (0.1 cm PWV, black), and a PWV-scaled U.S. Standard Atmosphere using data only above 5 km (0.04 cm PWV, red). The semitransparent microwindows contain important information about the water vapor line parameters,

[1] Atmospheric and Environmental Research, Inc., Lexington, Massachusetts, USA.
[2] Clough Radiation Associates, LLC, Lexington, Massachusetts, USA.
[3] Space Science and Engineering Center, Madison, Wisconsin, USA.
[4] Department of Environmental, Earth and Atmospheric Sciences, University of Massachusetts Lowell, Lowell, Massachusetts, USA.

0148-0227/10/2009JD012968

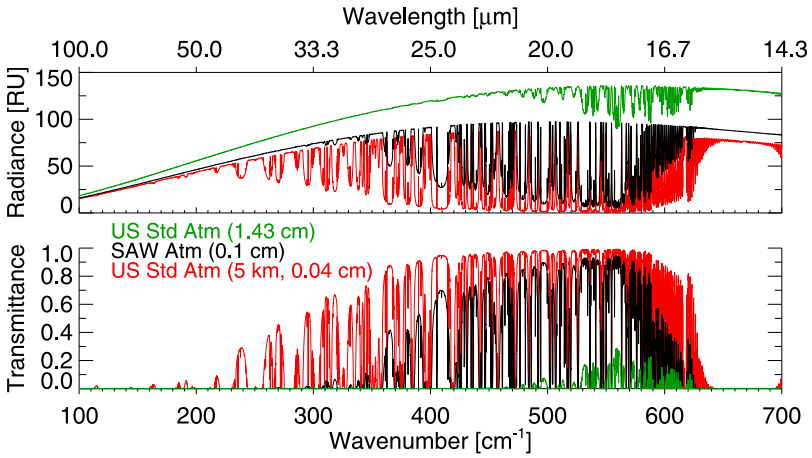

Figure 1. (top) The sensitivity of the calculated downwelling radiance received at the Earth's surface and (bottom) transmittance from surface to the top of the atmosphere. The three curves represent different water vapor loadings: U.S. Standard Atmosphere (1.43 cm PWV, green), PWV-scaled Subarctic Winter Atmospheric (0.1 cm PWV, black), and PWV-scaled U.S. Standard Atmosphere (0.04 cm PWV, red). The black line and red line represent expected results for RHUBC-I and RHUBC-II (altitude 5 km). A radiance unit (RU) equals 1 mW/(m^2 sr cm^{-1}).

including the intensity and widths, as well as the water vapor continuum absorption. Thus, ground-based measurement-model intercomparisons in low-PWV environments provide the opportunity to reduce the uncertainty in mid to upper tropospheric radiative transfer calculations in weather prediction and general circulation models [*Stamnes et al.*, 1999].

[4] Over the last two decades successful efforts have been put forth to obtain far-IR radiance measurements in very dry but logistically challenging locations. The landmark 1997 Surface Heat Budget of the Arctic (SHEBA) project [*Tobin et al.*, 1999; *Uttal et al.*, 2002] yielded ground-based, high–spectral resolution radiance measurements from the extended-range Atmospheric Radiance Emitted Interferometer (AERI-ER) [*Knuteson et al.*, 2004a] for comparison to Line-By-Line Radiative Transfer Model calculations (LBLRTM) [*Clough et al.*, 1992]. Using several observational time periods with a mean PWV of 0.34 cm, the strength of the foreign-broadened water vapor coefficients were significantly reduced (66% at 400 cm^{-1}) in the commonly used Clough-Kneiyzs-Davies water vapor continuum model (CKD) [*Clough et al.*, 1989]. However, the estimated 25% uncertainty in the water vapor profile used in the SHEBA analysis translated into an equivalent uncertainty in the continuum coefficients.

[5] Greatly expanding upon the SHEBA study, the Radiative Heating in Underexplored Bands Campaigns (RHUBC) are designed around simultaneous observations of atmospheric radiance and the atmospheric state. RHUBC field locations and observing times are chosen for their extreme dryness, thereby allowing spectroscopic information to be extracted from open microwindows from the far- to near-IR. RHUBC-I occurred at the U.S. Department of Energy Atmospheric Radiation Measurement Program's (ARM) North Slope of Alaska Climate Research Facility (NSA) [*Stokes and Schwarz*, 1994; *Ackerman and Stokes*, 2003] from 22 February to 14 March 2007. The NSA facility, located outside Barrow, Alaska, (N 71° 19′23.73″, W 156° 36′56.70″), was chosen not only because of its extensive instrument suite and user facility, but also because winter PWVs can dip to 0.1 cm (Figure 1, black). This paper presents results from a refinement of both the water vapor continuum model and water vapor line parameters in the far-IR using AERI-ER measurements from the RHUBC-I time period and additional clear sky periods from earlier in 2007. The PWV for each case was retrieved from the 183.31 GHz G-band Vapor Radiometer (GVR) permanently deployed at the site. The uncertainty in these PWV retrievals is approximately 2% [*Payne et al.*, 2008; *Cimini et al.*, 2009], a notable decrease in the PWV uncertainty compared to that obtained in the SHEBA experiment.

[6] The concept and components of this far-IR NSA radiative closure study are introduced in section 2. Analysis is presented in section 3, examining in detail the radiance residuals (measurements-model calculations) in the context of the radiometric measurements themselves as well as the specification of water vapor absorption in the forward model. As a result, the far-IR line parameters for many water vapor transitions and the water vapor continuum model have been updated. Synergies between the results of this study and those from the Earth Cooling by Water vapor Radiation (ECOWAR) Project [*Serio et al.*, 2008], a field campaign concurrent to RHUBC-I, will be discussed. The paper concludes with a discussion of the impact of far-IR forward model changes on net fluxes in the atmospheric column and a brief description of RHUBC-II, a field campaign that occurred in the Atacama Desert of Chile from August to October 2009. The minimum PWV at RHUBC-II (Figure 1, red) was over five times drier than those observed during this 2007 NSA study.

2. Far-IR Radiative Closure Study Components

[7] The concept for infrared radiative closure experiments using AERI radiance measurements from ARM climate research facilities and line-by-line radiative transfer model calculations was outlined by *Clough et al.* [1994] and has

Table 1. Description of Model Packages Referenced in Paper and Mean and Standard Deviation of Far-Infrared Residuals for That Model

Model Package	LBLRTM Version	Line Parameter Database	Continuum Module	Mean Residuals[b]	Standard Deviation Residuals[b]
LBL09	v11.6	aer_v_2.2[a]	MT_CKD_2.4	0.16	0.67
LBL06	v10.3	aer_v_1.1[a]	MT_CKD_1.2	0.82	1.10
LBL99	v5.10	HITRAN 1996	CKD_2.4.1	1.48	1.82

[a]Based on 2006 HITRAN.
[b]Measured in radiance units (RU) in the 400–625 cm^{-1} region.

been successfully used (1) to validate and improve continuum absorption models and spectral line parameters used in line-by-line models [e.g., *Turner et al.*, 2004a], (2) to assess the ability to define the atmospheric state used in the model calculations [e.g., *Turner et al.*, 2003; *Cady-Pereira et al.*, 2008], and (3) to assess the quality of the radiance observations themselves [e.g., *Turner*, 2003]. The design of the radiative closure experiment allows all three of these aspects to be simultaneously addressed. While these experiments can be used to investigate the absorption due to a variety of trace gases in all regions of the spectrum, the focus of this paper is an analysis of water vapor absorption parameters in the far-IR using AERI-ER measurements under clear skies at ARM NSA.

2.1. Line-by-Line Radiative Transfer Model and Associated Spectroscopic Parameters

[8] LBLRTM is an accurate and flexible radiative transfer model that can be used from the microwave to the ultraviolet. It has been used as the forward model for many retrieval algorithms [e.g., *Turner*, 2005; *Clough et al.*, 2006] and as the foundation from which rapid radiative transfer codes appropriate for use in climate models are built [e.g., *Mlawer et al.*, 1997]. The Voigt line shape is used at all pressures with an algorithm based on a linear combination of approximating functions, with a line cutoff at 25 cm^{-1} from line center [*Clough et al.*, 1989]. LBLRTM is more fully described by *Clough et al.* [2005]. Three LBLRTM packages are presented in this study: LBL99, LBL06, and LBL09 (where the digits refer to the year of model release). LBL99 and LBL06 are historical models and LBL09 is the model that has resulted from this work. The components of each model are listed in Table 1. In general, errors associated with computational procedures in LBLRTM are small, around five times less than those associated with available spectroscopic parameters. The limiting errors in spectral radiance calculations are attributable to the uncertainties in the line parameters, line shape, and the treatment of continua of different gases. A brief history of these parameters is discussed in the remainder of this section.

[9] The high-resolution transmission molecular database (HITRAN) is the primary source for the line parameters of all radiating molecules and absorption cross sections utilized by LBLRTM. A history of the parameters contained in HITRAN is given by *Rothman et al.* [2005, and references therein] and *Gordon et al.* [2007, and references therein]. According to *Gordon et al.* [2007], with regard to water vapor, HITRAN lists more than 64,000 significant transitions ranging from the microwave region to the visible, with intensities that cover many orders of magnitude. The water vapor half-width parameters have the largest dynamic range of any molecule contained in HITRAN; the uncertainties in these half-widths and in the line intensities have an important impact on the uncertainty estimates of radiative transfer calculations at tropospheric pressures, i.e., where collision broadening by air is significant.

[10] Over the last decade, water vapor transitions in HITRAN have been significantly updated, including the addition of thousands of lines and a large reduction in the uncertainties of the line positions, intensities, and air-broadened half-widths. Notably, *Gordon et al.* [2007] introduced new criteria for selecting the air-broadened half widths from all available measurements and theoretical calculations. The August 2006 HITRAN water vapor update file, 01_hit06.par, was incorporated into a complete line parameter database used in LBL06. This paper presents an evaluation of newly available water vapor line parameters, particularly the line intensities and air-broadened half widths, that have been incorporated into an updated line parameter database used in LBL09.

[11] Continuum absorption by water vapor also plays an important role in atmospheric radiative transfer. For many years no physical model was available to describe the observed water vapor continuum absorption. A key development in the understanding of this effect occurred with the introduction of the CKD continuum model [*Clough et al.*, 1989]. The original CKD model, CKD_0, was developed on the premise of a single line shape associated with each spectral line, one shape for foreign broadening (i.e., by dry air) and a second for self broadening (i.e., by water vapor). Over time a significant modification to this approach was implemented for two important reasons: (1) more degrees of freedom were required to fit the data than were available in the original line shape, and (2) the super-Lorentzian line shape in the intermediate wing region, within ~50 cm^{-1} from line center, was not supported by any known physics. To address these two issues a collision-induced component to the continuum was developed, replacing the super-Lorentzian characteristic of the CKD_0 line shape. This component provides the excess absorption observed in the central region of the vibrational bands, is characterized by its own line shape applied to each allowed spectral line, and in combination with the allowed component, provides the additional degrees of freedom necessary to fit observations. The collision-induced component is present in both the foreign and self continua. The primary impetus for this revision was to restore consistency between the formulation and the improved, measured continuum values; the new

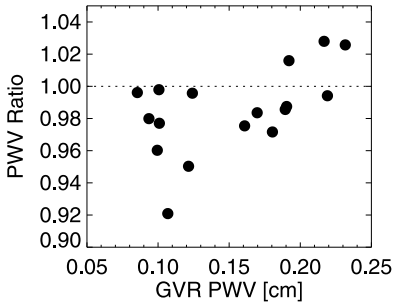

Figure 2. Ratios of radiosonde-derived to GVR-retrieved PWVs as a function of the GVR-retrieved PWV for 17 cases in cloud-free conditions at NSA from January to March 2007. The GVR PWV uncertainty is approximately 2%.

model was named Mlawer-Tobin Clough-Kneiyzs-Davies (MT_CKD) [*Clough et al.*, 2005].

[12] Modifications to the CKD and MT_CKD continuum models have historically been accomplished by applying spectral corrections to the original formulation in order to achieve improved agreement with observations. The most significant change to the original CKD foreign continuum model occurred as a consequence of the ground-based AERI-ER measurements made during SHEBA [*Tobin et al.*, 1999]. The spectral width of the pure rotational foreign-broadened water vapor continuum was narrowed significantly from that presented in CKD_0. This modification (CKD_2.4.1, LBL99) had significant implications for atmospheric cooling rates. MT_CKD_1.0 represented a completely new continuum formulation with changes throughout the entire spectrum. In the far-IR region of the AERI-ER data, 400 to 600 cm^{-1}, MT_CKD_1.0 diverged from CKD_2.4.1 as it respected SHEBA observations only in a limited set of microwindows near 420 cm^{-1}. MT_CKD_1.2 (LBL06) aimed to restore greater consistency with CKD_2.4.1. MT_CKD_2.1 was based on an early analysis of a subset of the current data and the reduction of the residuals was achieved solely by adjusting the continuum coefficients, ignoring the role of the line widths and pressure-induced line shift errors. The continuum model MT_CKD_2.4 (LBL09) that has resulted from this study takes such issues into account. For reference, plots of the historical continuum values are provided in section 3.2.2.

[13] Although not the focus of this paper, the far-IR is also influenced by the CO_2 ν_2 band, centered at 667 cm^{-1}. This band is an important tool used for remote sensing of atmospheric temperature, and consequently LBLRTM calculations in this band are continually subjected to validation tests [e.g., *Shephard et al.*, 2009]. In LBL06, only Q-branch line coupling was included. A key development between LBL06 and LBL09 has been the implementation of P-branch and R-branch line coupling, made possible by the extensive analysis and code developed by *Niro et al.* [2005]. With each CO_2 line coupling modification, the CO_2 continuum and CO_2 line shape have been modified although the line parameters have remained consistent with those in HITRAN 2000.

[14] In the context of this paper it is important to note that LBLRTM radiance calculations were part of a far-infrared model intercomparison [*Kratz et al.*, 2005]. In this comparison, LBLRTM calculations were consistent with other high-resolution models, but this study did not involve comparisons between models and measurements.

2.2. Characterization of the Atmospheric Profiles

2.2.1. Baseline Vertical Profiles

[15] Far-IR atmospheric radiative processes in clear skies are largely governed by the atmospheric temperature profile and vertical distribution of water vapor. For the model calculations performed in this study, Vaisala RS92 radiosondes provided the baseline vertical profiles for these two quantities in the troposphere and lower stratosphere. The thin-wire temperature sensor is calibrated at the factory with a stated uncertainty of 0.5°C; the relative humidity sensor is a thin-film capacitor with a stated uncertainty of 5%. Although far-IR radiance received at the surface is largely insensitive to the stratospheric properties, unrealistically large relative humidity values reported by the radiosonde above 9 km are set to climatological values. Above the maximum altitude reached by the radiosonde, standard climatological profiles are utilized for temperature and relative humidity. Climatological profiles were used for ozone, carbon monoxide, methane, nitrous oxide, chlorofluorocarbons, and nitric acid; the carbon dioxide mixing ratio was set to 390 ppmv.

[16] A 40 m meteorological tower with four in situ sensors of air temperature and relative humidity at 2, 10, 20, and 40 m above the surface is also present at NSA. For this study, a 5 min average of these measurements surrounding the sonde launch replaced the lowest points of the radiosonde measurements to best capture the air temperature inversion near the surface. In addition, in the lowest 1 km of the atmosphere where the temperature inversion is present, thin calculational layers were used in the radiative transfer model calculations to further resolve the temperature structure.

2.2.2. GVR Measurements and Water Vapor Profile Scaling

[17] Vaisala RS92 radiosondes, while improved from previous models, exhibit significant sonde-to-sonde variability in the calibration of their water vapor sensors as well as day/night biases [*Cady-Pereira et al.*, 2008; *Rowe et al.*, 2008; *Miloshevich et al.*, 2009]. In order to address this variability and systematic bias, other similar radiative closure studies have scaled the radiosonde profiles by a height-independent factor such that its scaled PWV matches that retrieved from a collocated microwave radiometer [*Turner et al.*, 2003; *Cady-Pereira et al.*, 2008]. In the dry environment of NSA, the 183.31 GHz water vapor line provides sufficient sensitivity for PWV retrievals (PWV $\leq$ 0.5 cm) [*Racette et al.*, 2005; *Cadeddu et al.*, 2007]. The GVR deployed at NSA [*Cadeddu et al.*, 2007] measures brightness temperature from four double sideband channels at 183.31 $\pm$ 1, 3, 7, 14 GHz with bandwidths of 0.5, 1.0, 1.4, and 2.0 GHz, respectively. The radiometer uses a hot (~330 K) and warm (~290 K) calibration target, and the calibration accuracy is approximately 1 K. The GVR measurements at NSA are prone to interference from a nearby U.S. Air Force radar system. A filter has been applied to remove this interference and these filtered data are available from the ARM archive.

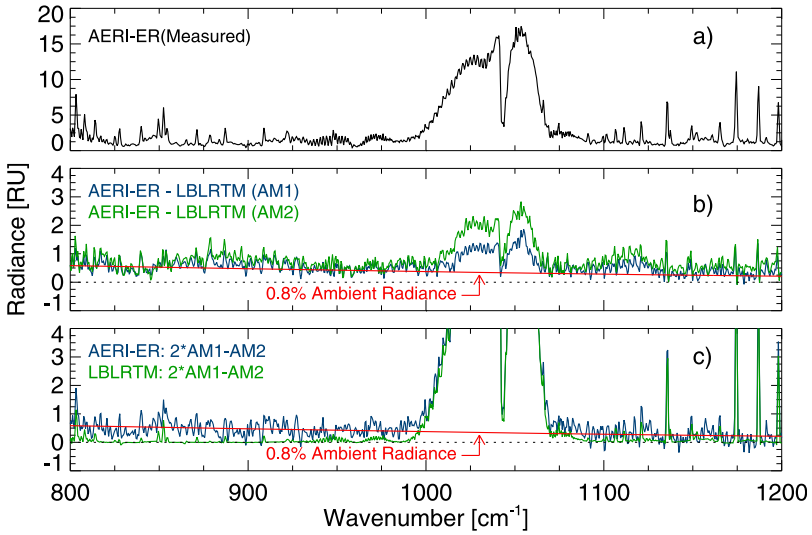

Figure 3. (a) Downwelling zenith radiance observed by the AERI at University of Wisconsin-Madison on 24 Jan 2008 at 1740 UTC, 0.11 cm PWV. (b) The difference between the observed and computed downwelling radiance at two elevation angles, zenith (1 airmass, AM1) and 60° off-zenith (2 airmasses, AM2). (c) The radiance determined by linearly extrapolating the observations and calculations from 2 and 1 airmasses to zero airmass. The red lines in Figures 3b and 3c denote 0.8% of the ambient radiance.

[18] As part of RHUBC-I, two additional 183 GHz radiometers were deployed: the ground-based scanning radiometer (GSR) [*Westwater et al.*, 2004] and the microwave profiler MP-183A [*Cimini et al.*, 2009]. The side-by-side operation of the three microwave radiometers provided an excellent opportunity to cross-compare measurements in a spectral region used extensively for remote sensing. In general, the instrument cross validation performed for sets of channel pairs, taking into account the different spectral characteristics, showed agreement within the total expected uncertainty. The consistency between instruments allow the determination of the PWV to within 2% for these dry conditions [*Cimini et al.*, 2009].

[19] An optimal estimation retrieval algorithm [*Rodgers*, 2000] was constructed to retrieve a PWV scaling factor for a radiosonde profile from the GVR 183.31 ± 7 GHz channel. MonoRTM [*Clough et al.*, 2005; *Payne et al.*, 2010], a monochromatic radiative transfer model incorporating similar physics to that in LBLRTM, was utilized as the forward model. The line parameters that significantly contribute to the retrieval, namely the intensity and air-broadened half-width, are described by *Clough et al.* [1973] and *Payne et al.* [2008]. Retrievals were performed only in atmospheric conditions free of liquid clouds and for cases in which the response of the brightness temperature to changes in PWV was linear (that is, brightness temperatures less than 100 K, roughly corresponding to PWV less than approximately 0.25 cm). The final water vapor profile for each case in this study is the baseline vertical profile scaled such that the total water vapor column matches the PWV retrieval from the coincident GVR measurements.

[20] For the time period of January through March 2007 at NSA, a PWV-scale factor was retrieved for each RS92 radiosonde profile used in this study. Figure 2 shows the ratio of the sonde PWV to the GVR-retrieved PWV as a function of the GVR-retrieved PWV for 17 cases. The mean ratio is 0.98 with a standard deviation of 0.02, demonstrating the degree of consistency between the radiosonde measurements and the GVR retrievals for this limited set of cases. All radiosondes utilized were launched when the sun was below the horizon, thereby the known daytime bias present in the Vaisala RS92 relative humidity measurements was not an issue. While the two sets of PWVs match well in the mean and have a reasonably small standard deviation for this limited set of cases, the GVR measurements were crucial to reducing the potential sonde-to-sonde variability due to calibration and other factors.

2.3. Atmospheric Emitted Radiance Interferometer

[21] The AERI is a ground-based Fourier transform spectrometer that measures the atmospheric downwelling radiance spectrum [*Knuteson et al.*, 2004a]. Designed and fabricated by the University of Wisconsin Space Science and Engineering Center for the ARM program, the AERI measures zenith radiance from 3020 cm^{-1} (3.3 μm) to 520 cm^{-1} (19 μm) at 0.5 cm^{-1} resolution with a calibration accuracy to better than 1% of the ambient radiance. Subsequently, an extended-range AERI-ER was developed specifically to cover the water vapor rotational band, measuring the atmospheric radiance down to 380 cm^{-1} (26 μm). The ARM program has deployed AERIs at each of its climate research facilities and mobile facility deployments, and over a decade of data has been collected.

[22] The AERI-ER utilizes a commercially available interferometer (Michelson series from ABB Bomem, Inc. of Quebec, Canada). The interferometer output is directed through two cryogenically cooled, stacked detectors: a shortwave InSb detector sensitive to radiation between 1800 cm^{-1} and 3020 cm^{-1} but insensitive to lower wavenumbers and a HgCdTe detector sensitive to radiation between 380 and

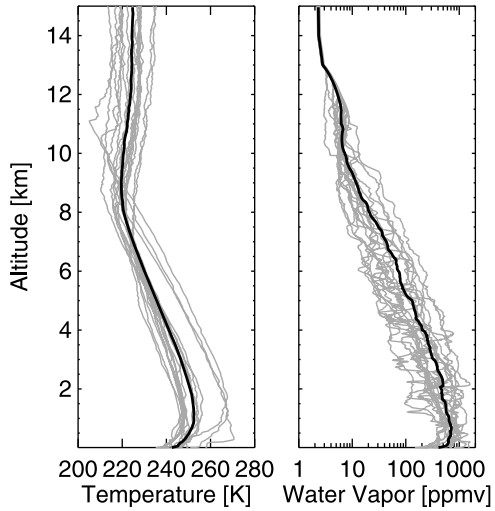

Figure 4. Atmospheric temperature and water vapor profiles for the NSA data set used in the measurement-model intercomparison. Grey lines show individual profiles, while the black lines represent the mean profile for the data set.

1800 cm^{-1} (referred to as AERI Channel 2 and Channel 1, respectively). Two high-emissivity, blackbody cavities at 60°C (hot) and ambient temperature, respectively, are used for radiometric calibration. Since the AERI calibration in clear sky scenes is an extrapolation from the hot and ambient blackbody temperatures to the colder sky temperature, uncertainties in either the temperature of the calibration blackbodies or the emissivity of these cavities can translate into uncertainties in the calibrated radiance. The uncertainties in the AERI blackbodies have been investigated in the laboratory, and these values are provided by *Knuteson et al.* [2004b, Table 3]. These uncertainties were propagated through the calibration equation to provide estimates of the random radiometric uncertainty; in general, the total radiometric uncertainty is less than 0.05 radiance units (RU) (1 $mW/(m^2\ sr\ cm^{-1})$) across the spectrum. Complete details on the AERI-ER are provided by *Knuteson et al.* [2004a, 2004b].

[23] The AERI-ER data used in this work have been postprocessed to reduce the uncorrelated random error in the data using principal component analysis [*Turner et al.*, 2006]. The data have been recalibrated from those obtained from the ARM data archive in order to account for an improved blackbody emissivity model [*Turner*, 2003]. An additional correction was made to the AERI-ER observed values near 400 cm^{-1} to account for small oscillations in the data generated in the processing of the interferograms. Because of noise and calibration considerations, only AERI-ER measurements above 400 cm^{-1} are used in this study.

[24] Clear-sky radiative closure studies between measured AERI radiances and LBLRTM calculations have been ongoing in the ARM program for more than a decade [*Clough et al.*, 1994; *Tobin et al.*, 1999; *Turner et al.*, 2004a]. These data sets have all demonstrated a similar, spectrally flat bias of approximately 1 RU between AERI and LBLRTM in

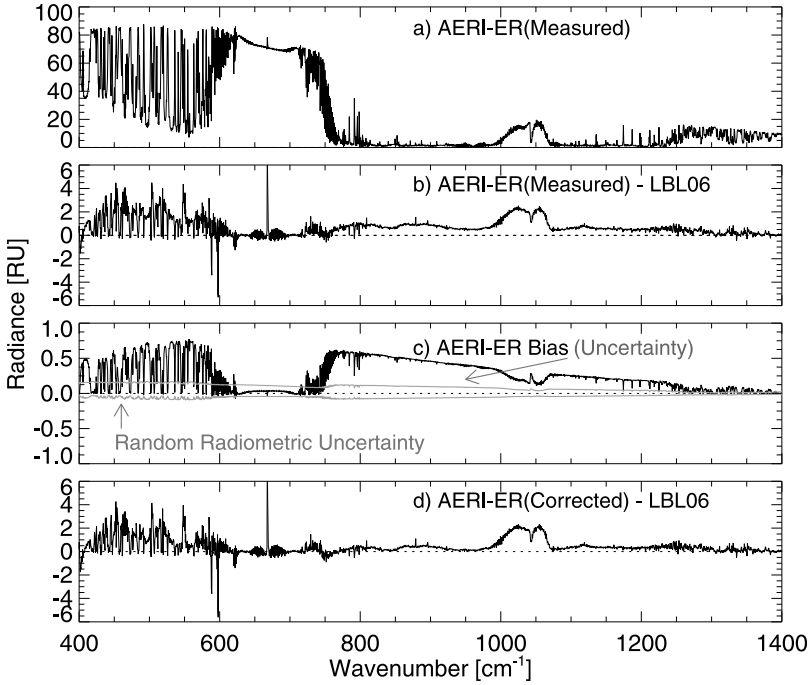

Figure 5. (a) Mean AERI-ER radiance for the NSA data set. (b) Mean spectral residuals between the original AERI-ER measurements and LBL06. (c) Mean AERI-ER radiance bias correction and uncertainty due to the warm-body obstruction (black line and top grey curve) and the random radiometric uncertainty estimate for a typical clear-sky AERI-ER observation (bottom grey curve). A value for the fractional obstruction of 0.010 was adopted and applied to all AERI-ER measurements. (d) Mean spectral residuals between the corrected AERI-ER measurements and LBL06.

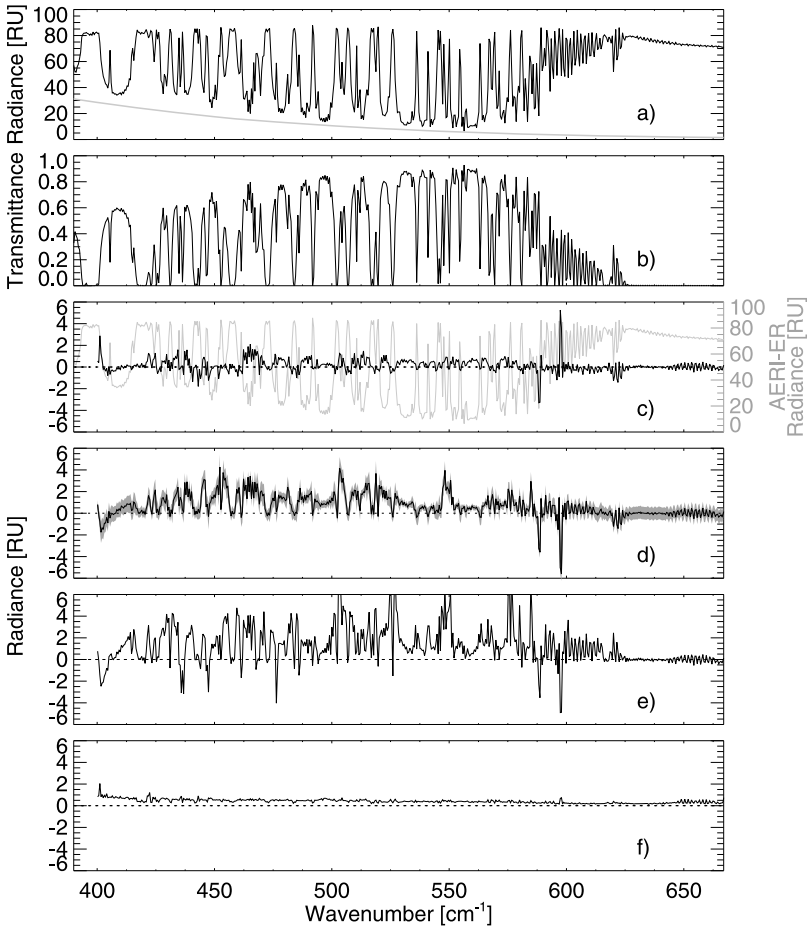

Figure 6. (a) Mean bias-corrected AERI-ER radiance for the NSA data set. The grey line represents the contribution of the water vapor continuum as calculated by LBL09. (b) Mean calculated transmittance for same cases. (c) Mean spectral residuals between the AERI-ER and LBL09. The grey line is the mean AERI-ER radiance. (d) Same as Figure 6c but using LBL06 calculations. The grey shading around the solid line represents the impact on the residuals due to systematic errors in the measured temperature profile and the total water vapor column. (e) Same as Figure 6c but using LBL99 calculations. (f) Standard deviation of spectral residuals for LBL09.

very low radiance conditions with the radiance measurement from the AERI being consistently higher [*Turner*, 2003, 2008]. *Turner* [2003] notes that radiosondes have considerable variability in their calibration but increasing the water vapor used in the calculations by a factor of two does not explain the residual nor does a large increase in the water vapor continuum coefficients. Because of its relatively flat spectral nature, errors associated with trace gas absorption do not explain the bias.

[25] As part of this research effort, multiple tests have been performed to evaluate the instrument alignment, sources of polarization, and the possibility of an obstruction in the field of view. Notably, an experiment was performed on 24 January 2008 at the University of Wisconsin-Madison (UW) to isolate the source of this bias. Under cloud-free, Arctic-type weather conditions (0.11 cm PWV, surface air temperature $< -15°C$), Vaisala RS92 radiosondes were released to characterize the atmospheric state. In this experiment, two AERI systems (both an extended-range and normal-range system) were modified to collect downwelling radiance data at zenith and 60° off zenith (i.e., at both 1 and 2 airmasses). The measured AERI-ER zenith radiance at 1740 UTC is shown in Figure 3a. The comparison of the AERI-ER radiance observations with LBLRTM calculations for both viewing angles is shown in Figure 3b. These plots indicate that in the most transparent microwindows the LBLRTM radiance calculations are significantly smaller than (i.e., roughly one third the magnitude of) the AERI measurements. A relatively smooth spectral bias of approximately 0.8% of the ambient radiance spectra is seen between the AERI-ER measurements and LBLRTM calculations. Note that the large residual centered at 1043 cm^{-1} is associated with ozone and not related to this analysis. A virtually identical bias was also observed in the normal-range AERI system (not shown). However, when the data collected/computed at the two airmass values is used to extrapolate to the top of the atmosphere (i.e., to zero airmass), the extrapolated radiance from the AERI-ER observations shows a bias that is the same 0.8% of the ambient radiance while the extrapolated radiance from the LBLRTM is zero (Figure 3c). This demonstrates conclusively that the bias is in the AERI-ER observations themselves. Unfortunately, this experiment,

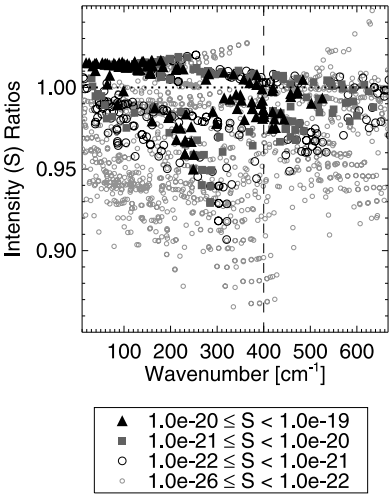

Figure 7. Ratios of the LBL06 main water vapor isotopologue intensities (S) to those in LBL09, grouped by their LBL09 intensities S (cm^{-1}/(molecule cm^{-2})) at 296 K. The vertical dashed line denotes the lower boundary of the AERI-ER spectral domain.

as well as subsequent experiments performed at UW, was unable to definitively identify the source of the bias in the AERI-ER observations, and work in this area continues.

[26] The AERI-ER instrument used in the UW experiment and the one at NSA were extensively compared side-by-side at NSA from January to May 2004 [*Turner et al.*, 2004b]. The resulting differences between the two instruments were significantly smaller than the bias above. Thus, the conclusions drawn from the experiment at UW are applicable to the NSA AERI-ER data set. An adjustment to the AERI-ER radiance measurements to account for this bias is described in section 3.

2.4. Data Set

[27] This analysis focuses on data collected in clear conditions at NSA from January 2007 through March 2007, which includes the field campaign RHUBC-I. Stringent criteria have been implemented for selecting cases for this study: cloud free, low PWV, and coincident radiosonde, GVR, and AERI-ER measurements of high quality. The detection of clouds, ice fog, and aerosols that are radiatively active in the far-IR is a known challenge at NSA. Data from the NSA micropulse lidar, millimeter cloud radar, and Vaisala ceilometer are combined to produce cloud base heights as part of ARM's Active Remote Sensing of Clouds Value-Added Product [*Clothiaux et al.*, 2000]. The ARSCL product, in combination with a visual inspection of micropulse lidar images, was used to cull out cloudy cases from the total set of radiosonde launches. Meeting the objectives of this study did not require tens to hundreds of cases, but rather several well-defined cases at sufficiently low PWV. As additional insurance that contaminated cases were not used and that the quality of the AERI-ER and GVRP data was good, cases that did not meet reasonable, clear-sky thresholds for the mean and standard deviation of the radiometric data over the chosen averaging window around the radiosonde launch time were eliminated. To account for the time taken by the radiosondes to ascend through the troposphere and lower stratosphere, the AERI-ER and GVR data were averaged for 35 min in each case (5 min before sonde launch, 30 min after launch).

[28] During this 3 month period, 206 radiosonde packages were launched: 84 during the 21 day RHUBC-I period and 122 on the remaining 69 days. Throughout this period, sondes were always launched at 0530 and 1730 UTC, consistent with the usual facility launch schedule at NSA. During RHUBC-I, additional sondes were launched in clear conditions. Of the 206 samples available, 17 met the criteria for inclusion into this measurement-model intercomparison. The mean surface air temperature for these cases was 242 K, ranging from 235 K to 258 K; the mean PWV derived from the GVR was 0.15 cm, ranging from 0.09 to 0.24 cm. The vertical profiles of temperature and water vapor volume mixing ratio are presented in Figure 4, illustrating the persistence of the strong near-surface temperature inversions that occasionally exceed 10 degrees in the lowest 1 km of the atmosphere.

3. Measurement-Model Comparisons

3.1. Overview

[29] An overall assessment of the residuals using AERI-ER Channel 1 measurements provides a necessary perspective for this far-IR radiative closure experiment. For the 17 cases in this data set, the average AERI-ER radiance spectrum is presented in Figure 5a. Water vapor emission is primarily responsible for the spectral features between 400 and 600 cm^{-1} (rotation band) and past 1200 cm^{-1} (ν_2 band). Other significant spectral features include the fundamental CO_2 bending mode centered at 667 cm^{-1} and the O_3 ν_3 band centered at 1043 cm^{-1}.

[30] The spectral residuals between the AERI-ER observations and LBL06 calculations are shown in Figure 5b. A small clear-sky bias is observed in the primary atmospheric window (800–1200 cm^{-1}), as described in section 2.3. The bias is removed using a technique that approximates a warm obstruction in the AERI-ER field of view [*Knuteson et al.*, 1999; *Turner*, 2003]. The radiance measured by the AERI-ER is given by

$$R_{m,v} = (1-f)R_{sky,v} + f\,\epsilon_v B_v\left(T_{eff}\right) \quad (1)$$

where $R_{m,v}$ is the measured radiance, $R_{sky,v}$ is the true sky radiance, B_v (T_{eff}) is the Planck contribution from the obstruction that has emissivity ϵ_v, and f is the fraction of the field of view obscured. Since no companion measurements are available from which to determine the true sky radiance, it is computed from LBLRTM calculations utilizing radiosonde profiles. The value used for T_{eff} is the temperature of the AERI-ER foreoptics (identified as the blackbody support structure temperature in the AERI-ER data files). Equation (1) can be inverted at each frequency v to obtain

$$f_v = \frac{R_{m,v} - R_{sky,v}}{\epsilon_v B_v\left(T_{eff}\right) - R_{sky,v}} \quad (2)$$

An average $f_{827\text{–}835}$ was derived for each case using a single microwindow from 827 to 835 cm^{-1} in which the uncertainty in the water vapor field or contamination from other

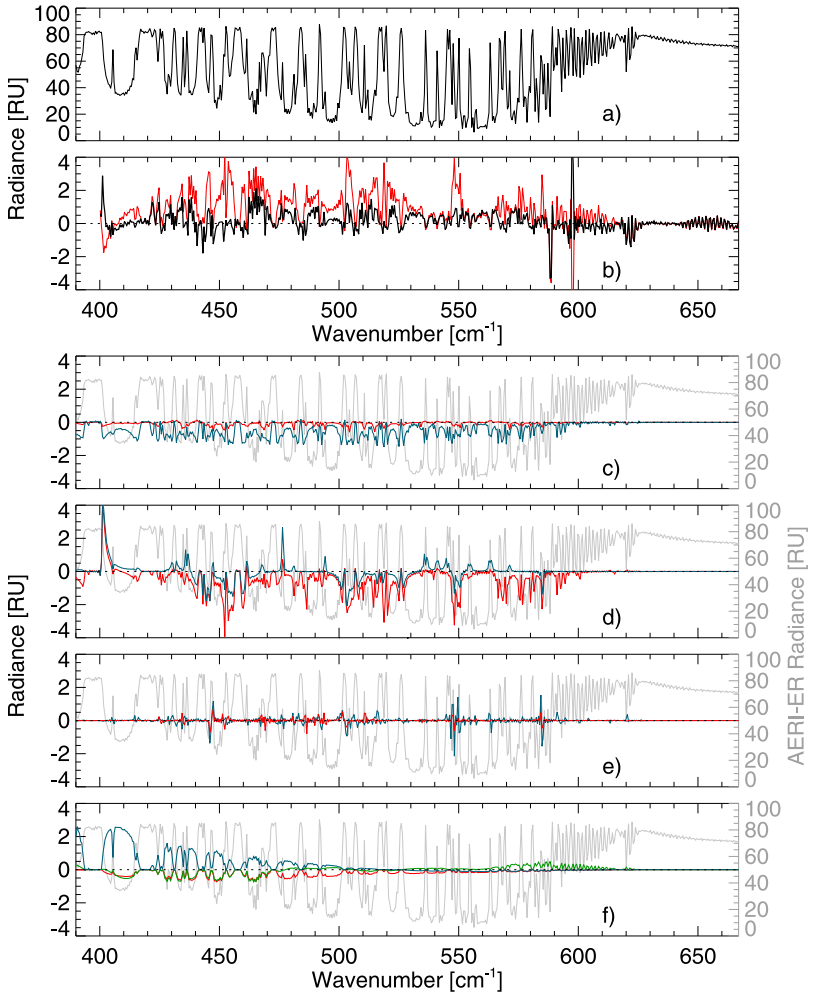

Figure 8. Mean difference in radiance calculations for the NSA data set due to perturbations in water vapor line parameters significant for far-IR radiative transfer calculations. Unless noted, all spectroscopic parameters and the water vapor continuum model are held fixed at LBL09. (a) Mean bias-corrected AERI-ER radiance for the NSA data set. (b) For reference, mean spectral residuals between the AERI-ER and model calculations using LBL09 (black) and LBL06 (red). (c) Calculational differences due to perturbed line intensities only (LBL06 minus LBL09, red; 5% perturbation to all LBL09 line intensities minus LBL09, blue). (d) Calculational differences due to perturbed air-broadened half-widths, temperature dependence exponents, and line shifts (LBL06 minus LBL09, red; CRB08 minus LBL09, blue). (e) Calculational differences due to perturbed line shifts only (LBL06 minus LBL09, red; no line shifts in LBL09 minus LBL09, blue). (f) Calculational differences due to perturbed water vapor continuum models only (LBL06 minus LBL09, red; MT_CKD_2.1 minus LBL09, blue; LBL99 minus LBL09, green). The light grey line in Figures 8c–8f is the mean AERI-ER radiance.

atmospheric constituents, such as chlorofluorocarbons, would be minimized. The fractional obstruction f was obtained using the first decile of retrieved $f_{827-835}$ values to ensure that the offset was not influenced by radiatively active aerosols or clouds that could have been missed in the case selection process. For this study, an f value of 0.010 with a 20% uncertainty (±0.002) was derived. This f was then applied to every spectral element of each AERI-ER observation to obtain corrected AERI-ER measurements,

$$R_{AERI-cor,v} = \frac{R_{m,v} - f\,\epsilon_v B_v(T_{eff})}{1-f} \quad (3)$$

The mean magnitude of the bias correction is less than 0.8 RU across the spectrum (black line) for the 17 cases is plotted in Figure 5c. For the bias correction derived for this study, the obstruction is assumed to have an emissivity of unity. Note that the uncertainty in this bias correction, accounting for a 20% uncertainty in f and allowing the emissivity to change from unity to that of the anodized aluminum in the AERI-ER front end, is less than 0.15 RU. The random radiometric uncertainty (section 2.3) associated with the extrapolation used in the calibration process is also plotted in Figure 5c, illustrating that the magnitude of the necessary radiance bias correction is larger than the random radiometric uncertainties. The radiance bias correction goes to zero in the

Table 2. Line Position, Air-Broadened Half-Widths γ_{air} From the Line Parameter Database Contained in LBL09, Ratios of γ_{air} (CRB08)/γ_{air} (LBL09), Ratios of γ_{air} (LBL06)/γ_{air} (LBL09), and Quantum Identification for 42 Transitions in the Water Vapor Rotation Band

Position	γ_{air} (LBL09)	γ_{air} (CRB08)/ γ_{air} (LBL09)	γ_{air} (LBL06)/ γ_{air} (LBL09)	J'	K'_a	K'_c	J''	K''_a	K''_c
400.2218	0.0400	1.978	1.965	10	4	6	9	3	7
400.4810	0.0350	1.457	1.457	10	6	4	9	5	5
417.6593	0.0606	1.111	0.931	11	5	6	10	4	7
431.1547	0.0852	1.032	1.021	6	4	2	5	1	5
436.4264	0.0209	1.086	0.923	9	9	1	8	8	0
436.4265	0.0209	1.086	0.923	9	9	0	8	8	1
441.7140	0.0819	1.053	1.042	5	5	0	4	2	3
442.0881	0.0952	0.909	0.898	6	5	2	5	2	3
443.6958	0.0373	0.909	0.885	10	8	3	9	7	2
443.7012	0.0373	0.909	0.882	10	8	2	9	7	3
446.3513	0.0441	0.971	0.927	11	7	5	10	6	4
446.9327	0.0428	0.972	0.923	11	7	4	10	6	5
447.4146	0.0560	1.191	1.098	13	6	8	12	5	7
452.8799	0.0795	0.952	0.896	11	4	7	10	3	8
456.8732	0.0909	0.926	0.923	7	5	3	6	2	4
457.7589	0.0765	0.925	0.910	9	2	7	8	1	8
457.7640	0.0789	0.926	0.923	10	3	7	9	2	8
461.4499	0.0254	1.087	1.012	10	9	2	9	8	1
461.4500	0.0254	1.087	1.012	10	9	1	9	8	2
467.8926	0.0335	1.042	0.854	11	8	4	10	7	3
467.9199	0.0334	1.042	0.943	11	8	3	10	7	4
476.4196	0.0162	1.253	1.012	10	10	1	9	9	0
476.4196	0.0162	1.253	1.012	10	10	0	9	9	1
478.0409	0.0519	1.156	1.160	4	4	1	4	4	0
481.0424	0.0493	1.053	0.834	13	6	7	12	5	8
494.1408	0.0341	1.176	0.953	13	7	6	12	6	7
502.2564	0.0618	0.934	0.921	10	4	7	9	1	8
504.3831	0.0786	0.885	0.790	13	5	8	12	4	9
506.9241	0.0783	0.962	0.945	7	5	2	6	2	5
515.0621	0.0317	1.088	0.896	13	8	5	12	7	6
516.7974	0.0723	0.971	0.959	10	5	6	9	2	7
517.7585	0.0627	0.962	0.943	10	2	8	9	1	9
525.9599	0.0556	0.962	0.941	10	3	8	9	0	9
536.2459	0.0772	1.053	1.039	6	6	1	5	3	2
541.0903	0.0743	1.052	1.036	6	6	0	5	3	3
545.2964	0.0799	1.053	1.039	8	4	4	7	1	7
547.8163	0.0650	0.943	0.832	11	5	7	10	2	8
550.0115	0.0531	0.944	0.859	11	4	8	10	1	9
554.6409	0.0791	1.030	1.018	7	6	2	6	3	3
563.2509	0.0843	1.052	1.023	6	5	2	5	0	5
571.2863	0.0600	1.053	0.995	13	4	9	12	3	10
584.7086	0.0561	0.925	0.854	12	5	8	11	2	9

most opaque regions of the spectrum and is greatest in the far-IR. Hereafter, all AERI-ER radiances presented have had the radiance bias correction applied.

[31] The spectral residuals, obtained with LBL06 and the corrected AERI-ER measurements, are presented in Figure 5d. The LBL06 residuals may be roughly divided into three spectral regions. First, the large residual centered at 1043 cm^{-1} is attributed to the incorrect distribution of ozone or stratospheric temperature in the input atmospheric profile. ARM does not routinely measure the column amount or ozone profile so a climatological value is used in this study; an improved ozone profile and stratospheric temperature profile would significantly reduce these residuals. The residuals between 600 and 780 cm^{-1} are associated with a combination of errors in the CO_2 ν_2 band absorption parameters in the model, the near-surface temperature specification, and, to a lesser extent, the water vapor spectroscopy and amount. This remains an active area of research. The third region of heightened LBL06 residuals is in the far-IR because of spectroscopic issues with respect to water vapor. The reduction of these residuals in the 400 to 600 cm^{-1} was the focus of this research effort.

3.2. Implications for the Radiative Transfer Model: 400–600 cm^{-1}

[32] For the 17 cases used in this analysis, the mean corrected far-IR AERI-ER radiances are presented in Figure 6a; Figure 6b shows the mean spectral transmittances calculated with LBL09. Figures 6c, 6d, and 6e demonstrate the far-IR spectral residuals from the current model (LBL09) and two historical model configurations (LBL06, LBL99); the standard deviation of these residual with respect to LBL09 is shown in Figure 6f. The components of the historical models were described in section 2.1. (A subset of this material is also shown in Figures 8a and 8b.) A strength of the NSA data set collected during the RHUBC period is the accuracy of the atmospheric state measurements. Unlike the SHEBA experiment in which the available measurement of

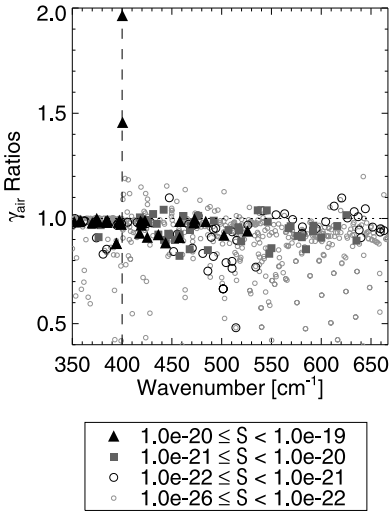

Figure 9. Ratios of the LBL06 main water vapor isotopologue air-broadened half-widths (γ_{air}) to those in LBL09, grouped by their LBL09 intensities S (cm^{-1}/(molecule cm^{-2})) at 296 K. The two large adjustments at 400 cm^{-1} simulate the impact of line coupling, unaccounted for by LBLRTM, on the radiance in the microwindow. The vertical dashed line denotes the lower boundary of the AERI-ER spectral domain.

PWV had an uncertainty of roughly 25%, the PWV retrieved from the 183.31 GHz GVR has an uncertainty of 2%. The stated temperature uncertainty from the Vaisala RS92 radiosondes is 0.5°C. Calculations with LBLRTM using input atmospheric state profiles containing these uncertainties yielded corresponding radiance uncertainties, shown by the grey shading in Figure 6d. It is evident that reasonable uncertainties in these input fields were not sufficient to explain the spectral residuals using LBL06.

[33] The sharp residual at 597 cm^{-1} is associated with carbon dioxide, arising from the inadequacy of the first-order treatment of the line coupling utilized by LBLRTM for the CO_2 Q-branch. The negative residual at 587 cm^{-1} is associated with line coupling in the Q-branch of nitrous oxide (N_2O), for which line coupling parameters are currently not available.

3.2.1. Water Vapor Line Parameter Analysis

[34] The far-IR water vapor line positions and line intensities in LBL06 are derived from several sources [*Rothman et al.*, 2003, 2005; *Gordon et al.*, 2007]. For the main isotopologue $H_2^{16}O$, LBL06 updated the line positions and intensities of 2582 lines involving the five first vibrational states between 0 and 800 cm^{-1} [*Coudert*, 1997, 1999; *Lanquentin et al.*, 2001; *Rothman et al.*, 2005]. Recently, *Coudert et al.* [2008] have updated their calculations from the far-IR through the ν_2 water vapor band centered at 1594.78 cm^{-1}, taking advantage of new measurements, measurements available from older literature, and a theoretical model. These updated water vapor positions and intensities have been adopted into LBL09 [*Shephard et al.*, 2009] from 10 to 2500 cm^{-1}. Figure 7 presents the ratio of line intensities utilized in LBL06 to those in LBL09 as a function of wave number across the far-IR (up to 667 cm^{-1}) and grouped by their new intensities at 296 K. For the strongest lines, the range of the ratios shown in Figure 7 is 0.95–1.02 whereas the ratios for the weaker lines span a wider range. Similarly, the ratios of the LBL06 to LBL09 line intensities are roughly 0.9 in the ν_2 band, leading to a significant improvement in water vapor retrievals that utilize data from this band (e.g., Infrared Atmospheric Sounding Instrument (IASI)) [*Shephard et al.*, 2009].

[35] The impact of the new Coudert line parameters on far-IR radiance calculations in the spectral domain of the AERI-ER is modest. The change in calculated radiances (referenced to LBL09) due to only the change in line intensities is plotted in Figure 8c (red). The strongest lines are already opaque as viewed from the ground, so a small change in their intensities would not be evident. Far from line centers in continuum-dominated regions (Figure 6a, grey line), there is also negligible response of the radiance to line intensity changes. For perspective, the effect of a 5% perturbation to all water vapor line intensities, corresponding to a maximum uncertainty stated in HITRAN for many of these lines, is shown in blue.

[36] The air-broadened half-widths (γ_{air}, HWHM at 296 K) for water vapor transitions of the main isotopologue used for the radiative transfer calculations are critical to the attainment of residuals consistent with the measurement accuracy. For the analysis presented here (Figure 8d) three sets of collisional width parameters from 350 to 667 cm^{-1} are evaluated.

[37] 1. LBL06 uses a combination of calculated values using the Complex Robert-Bonamy (CRB) method [*Gamache*, 2005], half-widths from the Toth database [*Toth*, 2005], or semiempirical values [*Jacquemart et al.*, 2005]. No γ_{air} measurements are included in the database because of data quality issues.

[38] 2. CRB08 contains updated CRB calculations the 350 to 667 cm^{-1} from the year 2008. Calculated values for the width temperature dependence and for the pressure-induced line shifts are also available for each transition.

[39] 3. LBL09 has been created in this study and is equivalent to CRB08 except for 42 transitions in which

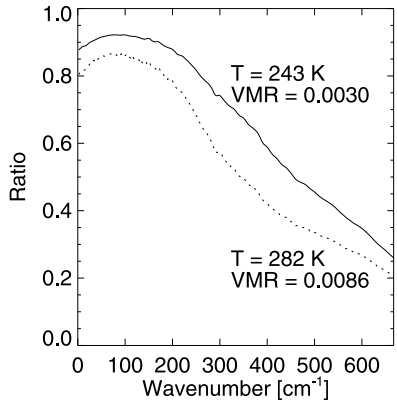

Figure 10. Ratio of the foreign-broadened water vapor continuum optical depth to the total continuum optical depth using MT_CKD_2.4 for two different temperatures and water vapor volume mixing ratios (VMR). T = 243 K is representative of the NSA cases used in this study; T = 282 K is representative of midlatitude conditions.

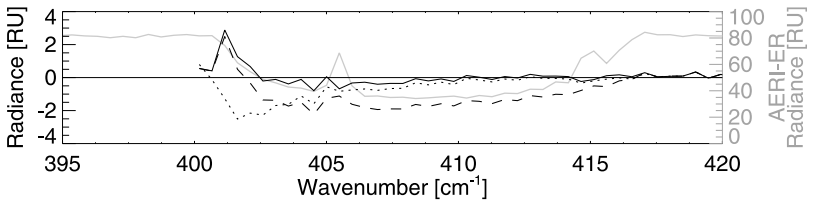

Figure 11. Mean spectral residuals for the NSA data set for various model configurations in a significant microwindow: LBL09 (solid black line), LBL09 but using CRB08 parameters (dotted line), and LBL09 but increasing the foreign-broadened water vapor continuum by 10% (dashed line). The grey line is the mean AERI-ER radiance. Modifications to the γ_{air} and the continuum coefficients have different spectral signatures, enabling their independent determination.

γ_{air} have been manually adjusted to minimize the spectral residuals. These 42 transitions are detailed in Table 2. The width adjustments have been made on the basis of the CRB08 temperature dependence. In specific cases the accuracy of the adjustments was limited by the effects of overlapping lines. Note that the radiating water vapor molecules are in the temperature regime from 270 K to 220 K, providing support for the width temperature dependences used. For six transitions the air pressure-induced line shift has been adjusted as well.

[40] The ratios of the γ_{air} in LBL06 to LBL09 are plotted Figure 9 as a function of wavenumber across the far-IR (up to 667 cm^{-1}) and grouped by their intensities. With the exception of two strong lines at 400 cm^{-1}, the γ_{air} values for lines of moderate to strong intensity generally increased between LBL06 and LBL09. Figure 8d presents the sensitivity of the calculated radiances to the adoption of the three sets of line widths, temperature dependence values, and line shifts described above. Figures 8b and 8d indicate CRB08 provides overall improvement over LBL06, particularly from 470 to 480 cm^{-1} and from 510 to 520 cm^{-1}. The adjusted line widths in LBL09 offer further reductions in the spectral residuals with respect to the AERI-ER measurements. Of particular interest is the region between 400 and 410 cm^{-1}, in which a consistently shaped residual was present in many of the cases analyzed (Figure 8b). This residual feature could not be explained by an error in the continuum alone. Investigation of the quantum number of these lines indicated that two of these lines are subject to the effects of line coupling [*Brown et al.*, 2005], which is not implemented in LBLRTM for water vapor. To mimic the impact of the line coupling on the microwindow radiance, the widths of two line-coupled lines were significantly reduced in LBL09. Further discussion of this large microwindow is given in section 3.2.2.

3.2.2. MT_CKD Continuum Analysis

[41] The continuum contribution to the spectral radiances for the conditions of the present study are shown by the grey curve in Figure 6a. In Figure 6a, spectral regions in which this curve is close to the measured radiances (black curve) are ones in which the continuum is the predominant absorber. Continuum coefficients are determined from radiances in these microwindows. Over the spectral region measured by the AERI-ER, there are five useful microwindows centered at 410, 477, 497, 533, and 560 cm^{-1}. Even in these microwindows, the accuracy of the continuum value is determined to a significant extent by our knowledge of the spectroscopic parameters of local lines. The microwindows at 447, 465, 489, 513, 566, and 576 cm^{-1} are not appropriate for the determination of the continuum because of the magnitude of the contributions from weak water lines in the windows with large intensity uncertainties.

[42] In the central regions of atmospheric water vapor bands the dominant continuum contribution is from the foreign continuum; between vibrational bands the dominant

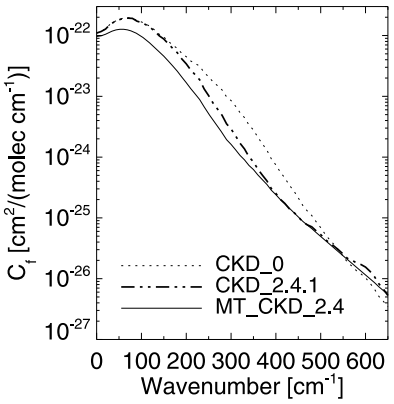

Figure 12. Foreign-broadened water vapor continuum coefficients, C_f, from various water vapor continuum models.

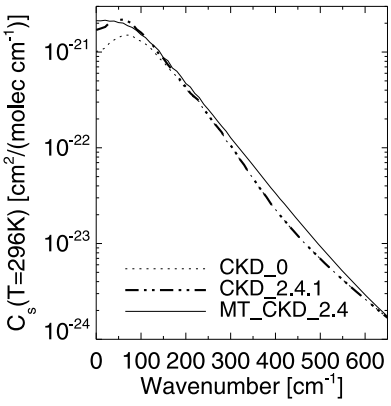

Figure 13. Self-broadened water vapor continuum coefficients, C_s, from various water vapor continuum models at T = 296 K.

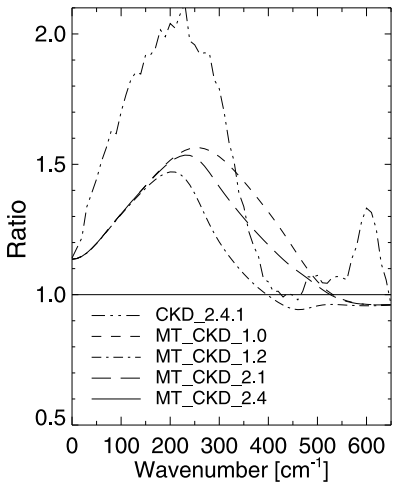

Figure 14. Ratio of the foreign-broadened water vapor continuum coefficients from recent continuum models to the new continuum model MT_CKD_2.4.

contribution is from the self continuum. This can be seen in Figure 10 in which the fraction of foreign continuum optical depth relative to the total continuum optical depth for MT_CKD_2.4 decreases from lower wavenumbers at the center of the pure-rotation band to higher wavenumbers on the edge of the band. The ratios for a typical NSA atmosphere (243 K) and a warmer, continental atmosphere (282 K) typical of the ARM Southern Great Plains Climate Research Facility are presented in Figure 10. Under the conditions relevant for the present study, the wavenumber at which the two components contribute equally in the continuum version shown is 470 cm^{-1}. Although both the foreign-broadened and the self-broadened continua contribute in the 400 to 600 cm^{-1} region, the range of observed PWVs during RHUBC-I does not provide sufficient information to parse with complete certainty the relative proportion of absorption between the two mechanisms. In this work, the changes in continuum optical depth needed for improving the residuals in this spectral region were assigned to the foreign continuum. With this assumption, the continuum changes herein are consistent with the decrease in the MT_CKD foreign continuum in the microwave region that followed from a study by *Payne et al.* [2010] and were confirmed by *Turner et al.* [2009].

[43] The updated formulation of the continuum that has been created as a result of this study, MT_CKD_2.4, was built from the base model MT_CKD_1.0. For MT_CKD_2.4, the self continuum was first adjusted using an analytic Pade function to accommodate new values of the self continuum in the microwave [*Payne et al.*, 2010], resulting in a 7% increase at 400 cm^{-1}. The temperature dependence of the self-continuum was not adjusted. A second Pade function was then developed for the foreign continuum to fit the new foreign continuum microwave value and the radiance values in the appropriate microwindows of the present data.

[44] The large microwindow at 400 cm^{-1} represents a region of particular interest with respect to the radiative transfer model. Mean spectral residuals for the NSA data set for various model configurations are shown in Figure 11: LBL09 (solid black line), LBL09 but using CRB08 parameters (dotted line), and LBL09 but increasing the foreign-broadened water vapor continuum by 10% (dashed line). The grey line is the mean AERI-ER radiance. It is apparent from this analysis that the spectral residuals associated with the CRB08 γ_{air}s (dotted line) in the vicinity of 402 cm^{-1} cannot be eliminated by a reasonable change to the foreign continuum alone. Attributed to the lack of water vapor line coupling in LBLRTM, the CRB08 residual was addressed by decreasing the γ_{air} values for the coupled lines thereby enabling a determination of the foreign continuum value in this spectral region.

[45] The updated foreign-broadened water vapor continuum coefficients presented here are in qualitative agreement with those retrieved as part of the ECOWAR project [*Bhawar et al.*, 2008]. The ECOWAR observations were collected from two sites at elevations of 2000 m and 3500 m, where the minimum PWV observed was 0.054 cm. *Serio et al.* [2008] retrieved the foreign-broadened water vapor continuum coefficients from 240 to 590 cm^{-1} and provided the first estimation of the water vapor continuum at wave numbers smaller than 400 cm^{-1} using data taken during a field campaign. Their results indicated that in the spectral region below 450 cm^{-1} radiances calculated using MT_CKD_2.1 overestimated the observations while above 450 cm^{-1} the agreement was good. *Serio et al.* [2008] recognized that there are line spectroscopy errors, but did not modify any line parameters in their work because of the fit they achieved in the nonwindow regions.

[46] For reference, the spectral values for the foreign-continuum and self-continuum coefficients (i.e., symmetrized power spectral density functions) for historical and current continuum versions are presented in Figures 12 and 13. Ratios of selected versions of the foreign-continuum coefficients and self-continuum coefficients to MT_CKD_2.4 are presented in Figures 14 and 15, respectively. The radiance differences due to three older continuum models with respect to MT_CKD_2.4 (LBL09) are shown in Figure 8f; all other

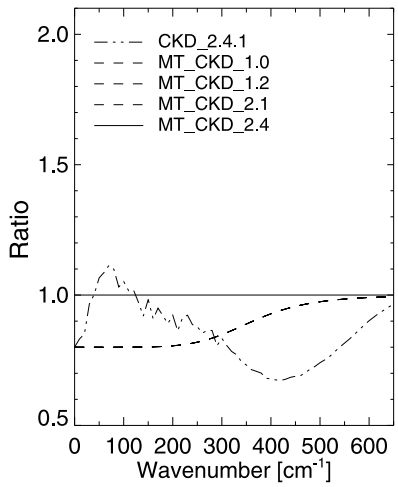

Figure 15. Ratio of the self-broadened water vapor continuum coefficients from recent continuum models to the new continuum model MT_CKD_2.4. MT_CKD_1.0, MT_CKD_1.2, and MT_CKD_2.1 are identical over this wavenumber range.

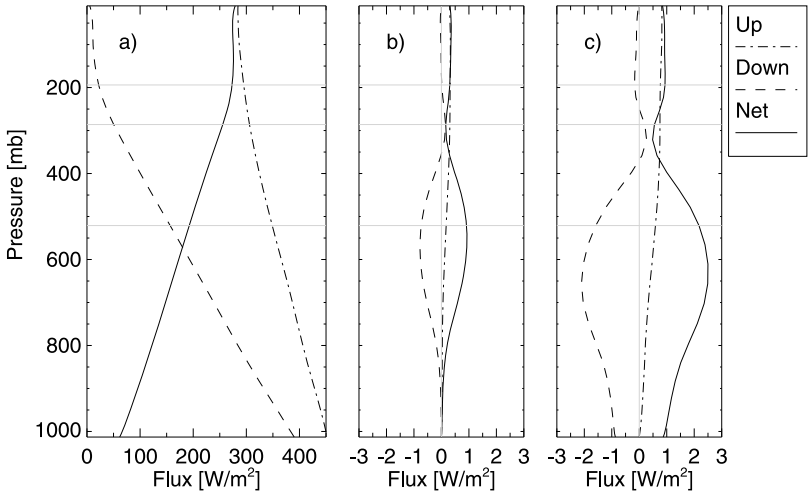

Figure 16. Impact of model revisions on clear-sky longwave fluxes (10–2000 cm^{-1}) for a standard tropical atmosphere. (a) Downwelling, upwelling, and net (up minus down) fluxes computed using LBL09. (b) Differences in computed fluxes (LBL06 minus LBL09). (c) Differences in computed fluxes (LBL99 minus LBL09). Grey lines are reference pressures used in spectral net flux calculations presented in Figure 17.

components used in the calculation remain the same. Examining Figure 8f, CKD_2.4.1 (green) and MT_CKD_1.2 (red) generate similar radiances throughout most of this spectral region although the two models have significant differences in the foreign-continuum and self-continuum coefficients (as shown in Figures 14 and 15). For MT_CKD_2.1 (blue), the foreign continuum change is sufficiently large that the model differences are strongly positive. It is important to note that the magnitude of these changes greatly exceeds the uncertainty (see Figure 5c) in the method used to account for the offset in the AERI-ER measurements.

4. Discussion

[47] The work presented here has resulted in a number of updates to far-IR water vapor line parameters and the water vapor continuum model used in LBLRTM. This region plays a critical role in atmospheric radiative processes but has until recently remained relatively understudied because of the opacity of the atmosphere above most ground-based research facilities and a lack of available instrumentation. Key advantages in the use of the data set presented here are the reduced uncertainty (~2%) in PWV provided by the collocated 183 GHz measurements and an improved correction method for determination of the AERI-ER instrument biases. For this ground-based data set, the mean measurement-model radiance difference and its standard deviation from 400 to 625 cm^{-1} have been significantly decreased between the 2006 and 2009 model calculations (Table 1).

[48] The recommendations on water vapor spectroscopy that have resulted from this work are a subset of the total spectroscopic improvements that have been incorporated into LBLRTM and its components over the last few years. To illustrate the overall changes to the motel, LBL09 was used to compute vertical flux profiles for a standard tropical atmosphere. Absorption by water vapor, carbon dioxide, ozone, nitrous oxide, carbon monoxide, methane, oxygen, and nitrogen have been accounted for in the model calculations. The upwelling, downwelling, and net (upwelling-downwelling) longwave fluxes for spectral interval 10–2000 cm^{-1} are presented in Figure 16a. The effects of using historical models to calculate the fluxes are demonstrated in Figures 16b (LBL06 minus LBL09) and 16c (LBL99 minus LBL09). The maximum net flux differences occur between 500 and 600 mbars.

[49] While the total net flux plots are informative, a more complete story of the model and its uncertainties is told by examining the spectral contribution to the total net fluxes for the various models. Figure 17 demonstrates the spectral net flux differences between models calculated for the same tropical atmosphere at three pressure levels (denoted by the horizontal grey lines in Figure 16). Figure 17a shows the net flux differences between two model configurations (LBL06 minus LBL09, black line; LBL99 minus LBL09, grey line) at 521 mbars. Figure 17b demonstrates the net flux differences due to water vapor continuum model changes only (LBL06 minus LBL09, black line; LBL99 minus LBL09, grey line), holding all other parameters fixed at LBL09. The differences are nearly all positive in Figure 17a; from 400 cm^{-1} to 600 cm^{-1} the net flux differences are attributed primarily to changes in water vapor line parameters with a modest contribution from the continuum changes. Beyond 600 cm^{-1}, the changes are attributed to a new treatment of carbon dioxide absorption processes.

[50] Moving into the upper troposphere to 286 mbars, as shown in Figures 16b and 16c, the total net flux difference between the models is nearly zero. However, this integrated net flux masks spectral differences due to a significant amount of model development that has occurred throughout the far-IR and into the midinfrared. The large negative change in net flux between 150 to 400 cm^{-1} is matched by a positive change in net flux beyond 400 cm^{-1} (Figure 17c). The bulk of the change below 400 cm^{-1} is almost entirely due to changes in the treatment of the water vapor continuum (Figure 17d). In the region between 100 and 400 cm^{-1},

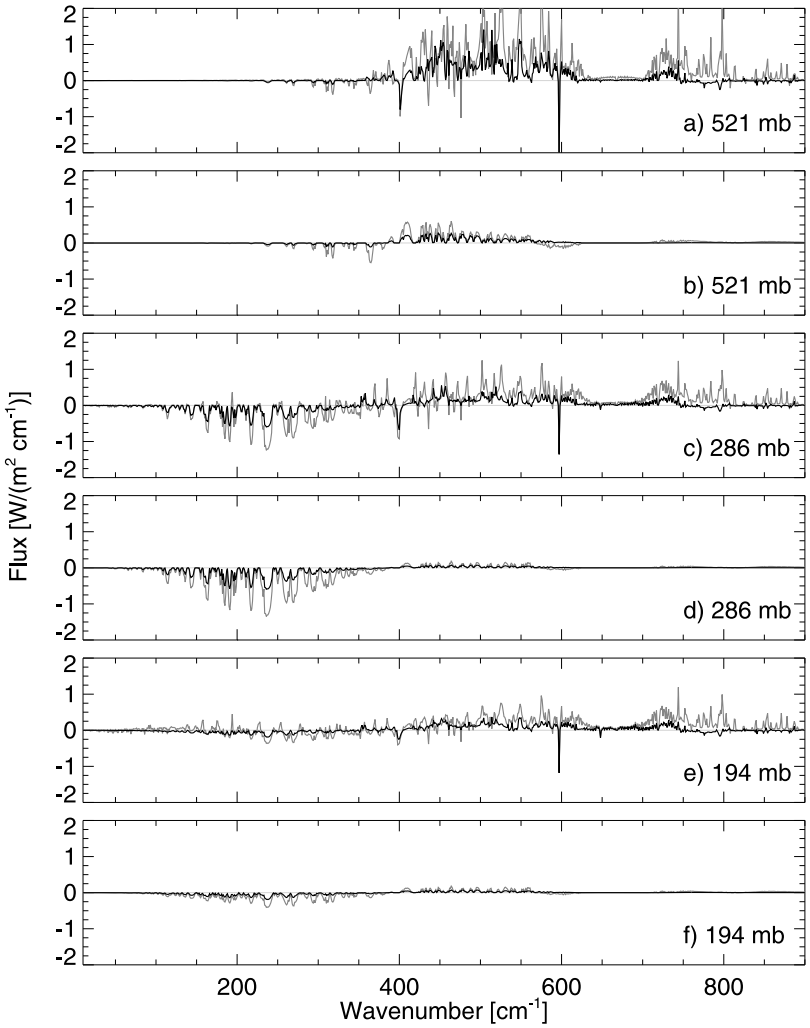

Figure 17. Spectral net flux differences for a standard tropical atmosphere at given pressure levels and for various model versions. (a) Net flux differences at 521 mbars (LBL06 minus LBL09, black; LBL99 minus LBL09, grey). (b) Net flux differences at 521 mbars due to continuum model change only (LBL06 minus LBL09, black; LBL99 minus LBL09, grey), holding all other parameters fixed at LBL09. (c) Same as Figure 17a but at 286 mbars. (d) Same as Figure 17b but at 286 mbars. (e) Same as Figure 17a but at 194 mbars. (f) Same as Figure 17b but at 194 mbars.

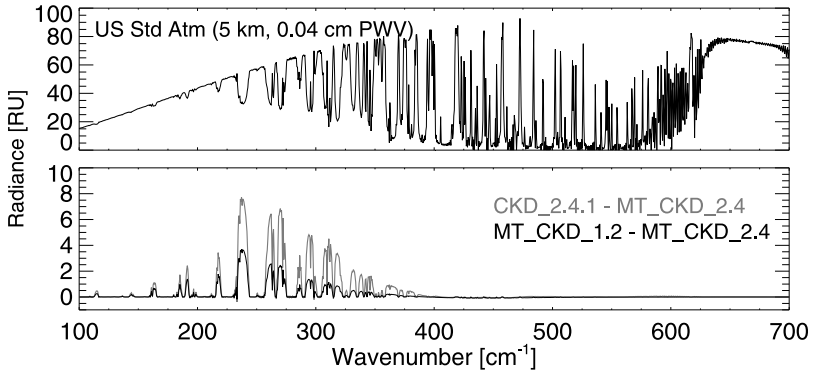

Figure 18. (top) The sensitivity of the LBL09-calculated downwelling radiance to (bottom) different versions of the water vapor continuum model for a PWV-scaled U.S. Standard Atmosphere (0.04 cm PWV) truncated at 5 km. All other model parameters remain fixed at LBL09.

there is a dearth of measurements and the continuum model has been determined by analytic continuation of the continuum values determined in this study and in the microwave [*Turner et al.*, 2009; *Payne et al.*, 2010]. This places significant uncertainty on any flux calculations in this spectral region, which translates into uncertainty in climate model simulations. As the transition is made to 194 mbars (Figures 17e and 17f), the changes between models in net flux calculations appear to be driven by adjustments in the treatment of CO_2 line coupling.

[51] It is anticipated that the second phase of the RHUBC campaign will be key to the reduction of far-IR uncertainties in the simulation of midtropospheric to upper tropospheric radiative processes due to water vapor. This is particularly important given the increase in upper tropospheric humidity over the last two decades [*Solomon et al.*, 2007]. RHUBC-II took place in the Atacama Desert, Chile in conditions that were five times drier than the minimum observed during RHUBC-I at NSA in 2007 [*Turner and Mlawer*, 2010]. A complete suite of meteorological instruments, microwave radiometers, and high-resolution far-IR radiometers measuring down to 10 cm^{-1} were deployed from August to October 2009. In such conditions (PWV < 0.05 cm), most spectral regions impacting the upper tropospheric heating rates have semitransparent microwindows (Figure 1) in which the determination of accurate water vapor continuum coefficients and other spectroscopic parameters can be made. For example, Figure 18 shows radiances computed with different versions of the water vapor continuum models for the RHUBC-II simulation atmosphere (U.S. Standard Atmosphere, truncated at 5 km, 0.04 cm PWV). The RHUBC-II data will provide a significant set of measurements to fill the data gap between the AERI-ER observations and those in the microwave and will help to pin down the absorption properties of water vapor throughout the far-IR.

[52] LBLRTM, water vapor continuum models, and line parameter databases as well as a historical description of each are publicly available from the Atmospheric & Environmental Research, Inc. Web site (http://rtweb.aer.com) or from the corresponding author. The line parameter databases associated with the model packages LBL06 and LBL09 are identified as *aer_v_*1.1 and *aer_v_*2.2 on the host Web site. HITRAN line files are available from http://www.hitran.com. ARM data are freely available via the ARM data archive (http://www.archive.arm.gov). Additional information regarding the RHUBC campaign can be found at http://acrf-campaign.arm.gov/rhubc/.

[53] **Acknowledgments.** Data were obtained from the Atmospheric Radiation Measurement (ARM) Program sponsored by the U.S. Department of Energy, Office of Science, Office of Biological and Environmental Research, Environmental Sciences Division. This research was funded by the DOE ARM program grants DE-FG02-05ER639 and DE-FG02-06ER64167. R. R. Gamache is pleased to acknowledge support of this research by the National Science Foundation through grant ATM-0803135. We would like to thank R. Knuteson, D. Hackel, R. Dedecker, N. Ciganovich, F. Best, and H. Revercomb for their assistance and input regarding the rooftop test of the AERI-ER at the University of Wisconsin-Madison. Comments from two anonymous reviewers were greatly appreciated.

References

Ackerman, T., and G. Stokes (2003), The Atmospheric Radiation Measurement Program, *Phys. Today*, *56*, 38–45.

Bhawar, R., et al. (2008), Spectrally resolved observations of atmospheric emitted radiance in the H_2O rotation band, *Geophys. Res. Lett.*, *35*, L04812, doi:10.1029/2007GL032207.

Brown, L., D. Benner, V. Malathy-Devi, and M. Smith (2005), Line mixing in self- and foreign-broadened water vapor at 6 μm, *J. Mol. Struct.*, *742*, 111–122.

Cadeddu, M., J. Liljegren, and A. Pazmany (2007), Measurements and retrievals from a new 183-GHz water vapor radiometer in the Arctic, *IEEE Trans. Geosci. Remote Sens.*, *45*, 2207–2215.

Cady-Pereira, K. E., M. Shephard, D. Turner, E. Mlawer, S. Clough, and T. Wagner (2008), Improved daytime precipitable water vapor from Vaisala radiosonde humidity sensors, *J. Atmos. Oceanic Technol.*, doi:10.1175/2007JTECHA1027.1.

Cimini, D., F. Nasir, E. R. Westwater, V. H. Payne, D. D. Turner, E. J. Mlawer, M. L. Exner, and M. P. Cadeddu (2009), Comparison of ground-based millimeter-wave observations and simulations in the Arctic winter, *IEEE Trans. Geosci. Remote Sens*, *47*, 3098–3106, doi:10.1109/TGRS.2009.2020743.

Clothiaux, E., T. Ackerman, G. Mace, K. Moran, R. Marchand, M. Miller, and B. Martner (2000), Objective determination of cloud heights and radar reflectivities using a combination of active remote sensors at the arm cart sites, *J. Appl. Meteorol.*, *39*, 645–665.

Clough, S., Y. Beers, J. Klein, and L. Rothman (1973), Dipole moment of water from Stark measurements of H_20, HDO, and D_2O, *J. Chem. Phys.*, *59*, 2254.

Clough, S., F. Kneizys, and R. Davies (1989), Line shape and the water vapor continuum, *Atmos. Res.*, *23*, 229–241.

Clough, S., M. Iacono, and J. Moncet (1992), Line-by-line calculations of atmospheric fluxes and cooling rates: Application to water vapor, *J. Geophys. Res.*, *97*, 15,761–15,785.

Clough, S., P. Brown, N. Miller, J. Liljegren, and T. Shippert (1994), Residual analysis of surface spectral radiances between instrument observations and line-by-line calculations, in *Proceedings of the Fourth Atmospheric Radiation Measurement (ARM) Science Team Meeting*, U.S. Dep. of Energy, Washington, D. C.

Clough, S. A., M. W. Shephard, E. J. Mlawer, J. S. Delamere, M. J. Iacono, K. Cady-Pereira, S. Boukabara, and P. D. Brown (2005), Atmospheric radiative transfer modeling: A summary of the AER codes, *J. Quant. Spectrosc. Radiat. Transfer*, *91*, 233–244.

Clough, S., et al. (2006), Forward model and Jacobians for Tropospheric Emission Spectrometer retrievals, *IEEE Trans. Geosci. Remote Sens.*, *44*, 1308–1323.

Coudert, L. (1997), Analysis of the line positions and line intensities in the ν_2 band of the water molecule, *J. Mol. Spectrosc.*, *181*, 246–273.

Coudert, L. (1999), Line frequency and line intensity analyses of water vapour, *Mol. Phys.*, *96*, 941–954.

Coudert, L., G. Wagner, M. Birk, Y. Baranov, W. Lafferty, and J.-M. Flaud (2008), The $H_2^{16}O$ molecule: Line position and line intensity analyses up to the second triad, *Mol. Phys.*, *96*, 941–954.

Gamache, R. (2005), Line shape parameters of water vapor in the 3.2–17.76 μm region for atmospheric applications, *J. Mol. Spectrosc.*, *229*, 9–18.

Gordon, I., L. Rothman, R. Gamache, D. Jacquemart, C. Boone, P. Bernath, M. Shephard, J. Delamere, and S. Clough (2007), Current updates of the water-vapor line list in *HITRAN*: A new "diet" for air-broadened half-widths, *J. Quant. Spectrosc. Radiat. Transfer*, *108*, 389–402.

Harries, J., B. Carli, R. Rizzi, C. Serio, M. Mlynczak, L. Palchetti, T. Maestri, H. Brindley, and G. Masiello (2008), The far-infrared Earth, *Rev. Geophys.*, *46*, RG4004, doi:10.1029/2007RG000233.

Jacquemart, D., R. Gamache, and L. Rothman (2005), Semi-empirical calculation of air-broadened half-widths and air pressure-induced frequency shifts of water vapor absorption lines, *J. Quant. Spectrosc. Radiat. Transfer*, *96*, 205–239.

Knuteson, R., B. Whitney, H. Revercomb, and F. Best (1999), The history of the University of Wisonsin Atmospheric Emitted Radiance Interferometer (AERI) Prototype during the period of April 1994 through July 1995, *Tech. Rep. ARM TR-001.1*, U.S. Dep. of Energy, Washington, D. C.

Knuteson, R., et al. (2004a), Atmospheric Emitted Radiance Interferometer. Part I: Instrument design, *J. Atmos. Oceanic Technol.*, *21*, 1763–1776.

Knuteson, R., et al. (2004b), Atmospheric Emitted Radiance Interferometer. Part II: Instrument performance, *J. Atmos. Oceanic Technol.*, *21*, 1777–1789.

Kratz, D., M. Mlynczak, C. Mertens, H. Brindley, L. Gordley, J. Martin-Torres, F. Miskolczi, and D. Turner (2005), An inter-comparison of far-infrared line-by-line radiative transfer models, *J. Quant. Spectrosc. Radiat. Transfer*, *90*, 323–341.

Lanquentin, R., L. Coudert, and C. Camy-Peret (2001), High-lying rotational levels of water: An analysis of the energy levels of the five first vibrational states, *J. Mol. Spectrosc.*, *206*, 83–103.

Miloshevich, L., H. Vomel, D. Whiteman, and T. Leblanc (2009), Accuracy assessment and correction of Vaisala RS92 radiosonde water vapor measurements, *J. Geophys. Res.*, *114*, D11305, doi:10.1029/2008JD011565.

Mlawer, E., S. Taubman, P. Brown, M. Iacono, and S. Clough (1997), Radiative transfer for inhomogeneous atmospheres: RRTM, a validated correlated-k model for the longwave, *J. Geophys. Res.*, *102*, 16,663–16,682.

Niro, F., K. Jucks, and J. Hartmann (2005), Spectral calculations in central and wing regions of CO_2 IR bands. IV: Software and database for the computation of atmospheric spectra, *J. Quant. Spectrosc. Radiat. Transfer*, *95*, 469–481.

Payne, V., J. Delamere, K. Cady-Pereira, R. Gamache, J. Moncet, E. Mlawer, and S. Clough (2008), Air-broadened half-widths of the 22 GHz and 183 GHz water vapor lines, *IEEE Trans. Geosci. Remote Sens.*, *46*, 3601–3617.

Payne, V., E. Mlawer, K. Cady-Pereira , and J. L. Moncet (2010), Water vapor continuum absorption in the microwave, *IEEE Trans. Geosci. Remote Sens.*, in press.

Racette, P., et al. (2005), Measurements of low amounts of precipitable water vapor using ground-based millimeterwave radiometry, *J. Atmos. Oceanic Technol.*, *22*, 317–337.

Rodgers, C. (2000), *Inverse Methods for Atmospheric Sounding: Theory and Practice*, World Sci., Singapore.

Rothman, L., et al. (2003), The HITRAN molecular spectroscopic database: Edition of 2000 including updates through 2001, *J. Quant. Spectrosc. Radiat. Transfer*, *82*, 5–44.

Rothman, L., et al. (2005), The HITRAN 2004 molecular spectroscopic database, *J. Quant. Spectrosc. Radiat. Transfer*, *96*, 139–204.

Rowe, P., L. Miloshevich, D. Turner, and V. Walden (2008), Dry bias in Viasala RS90 radiosonde humidity profiles over Antarctica, *J. Atmos. Oceanic Technol.*, *25*, 1529–1541.

Serio, C., et al. (2008), Retrieval of foreign-broadened water vapor continuum coefficients from emitted spectral radiance in the H_2O rotational band from 240 to 590 cm^{-1}, *Opt. Express*, *16*, 15,816–15,833.

Shephard, M., S. Clough, V. Payne, W. Smith, S. Kireev, and K. Cady-Pereira (2009), Evaluation of the line-by-line radiative transfer model (LBLRTM) with spectral satellite measurements: IASI case studies from JAIVEx, *Atmos. Chem. Phys.*, *9*, 9313–9366.

Sinha, A., and J. Harries (1995), Water vapour and greenhouse trapping: The role of far infared absorption, *Geophys. Res. Lett.*, *22*, 2147–2150.

Solomon, S., D. Qin, M. Manning, Z. Chen, M. Marquis, K. Averyt, M. Tignor, and H. Miller (Eds.) (2007), *Climate Change* 2007*: The Physical Science Basis: Contribution of Working Group I to the Fourth Assessment Report on the Intergovernmental Panel on Climate Change*, Cambridge Univ. Press, Cambridge, U. K.

Stamnes, K., R. Ellingson, J. Curry, J. Walsh, and B. Zak (1999), Review of science issues, deployment strategy, and status for the ARM North Slope of Alaska—Adjacent Arctic Ocean climate research site, *J. Clim.*, *12*, 46–63.

Stokes, G., and S. Schwarz (1994), The Atmospheric Radiation Measurement program: Programmatic background and design of the cloud and radiation test bed, *Bull. Amer. Meteorol. Soc.*, *75*, 1201–1221.

Tobin, D., et al. (1999), Downwelling spectral radiance observations at the SHEBA ice station: Water vapor continuum measurements from 17 to 26 μm, *J. Geophys. Res.*, *104*, 2081–2092.

Toth, R. (2005), Measurements and analysis (using empirical functions for widths) of air- and self-broadening parameters of H_2O, *J. Quant. Spectrosc. Radiat. Transfer*, *94*, 1–50.

Turner, D. (2003), Microphysical properties of single and mixed-phased Arctic clouds derived from ground-based AERI observations, Ph.D. thesis, Univ. of Wisconsin-Madison, Madison. (Available at http://www.ssec.wisc.edu/turnerdissertation.pdf.)

Turner, D. (2005), Arctic mixed-phase cloud properties from AERI lidar observations: Algorithm and results from SHEBA, *J. Appl. Meteorol.*, *44*, 427–444.

Turner, D. (2008), Ground-based retrievals of optical depth, effective radius, and composition of airborne mineral dust above the Sahel, *J. Geophys. Res.*, *113*, D00E03, doi:10.1029/2008JD010054, [printed 114(D13), 2009].

Turner, D., and E. Mlawer (2010), The Radiative Heating in Underexplored Bands Campaigns, *Bull. Amer. Meteorol. Soc.*, *91*, 911–923, doi:10.1175/2010BAMS2904.1.

Turner, D., B. Lesht, S. Clough, J. Liljegren, H. Revercomb, and D. Tobin (2003), Dry bias and variability in Vaisala radiosondes: The ARM experience, *J. Atmos. Oceanic Technol.*, *20*, 117–132.

Turner, D. D., et al. (2004a), The QME AERI LBLRTM: A closure experiment for downwelling high spectral resolution infrared radiance, *J. Atmos. Sci.*, *61*, 2657–2675.

Turner, D., H. Revercomb, R. Knuteson, R. Dedecker, and W. Feltz (2004b), An evaluation of the nonlinearity correction applied to Atmospheric Emitted Radiance Interferometer (AERI) data collected by the Atmospheric Radiation Measurement Program, *Tech. Rep. ARM TR-013*, U.S. Dep. of Energy, Washington, D. C.

Turner, D., R. Knuteson, H. Revercomb, C. Lo, and R. Dedecker (2006), Noise reduction of Atmospheric Emitted Radiance Interferometer (AERI) observations using principal component analysis, *J. Atmos. Oceanic Technol.*, *23*, 122–1238.

Turner, D., U. Lohnert, M. Cadeddu, S. Crewell, and A. Vogelmann (2009), Modifications to the water vapor continuum in the microwave suggested by ground-based 150-GHz observations, *IEEE Trans. Geosci. Remote Sens.*, *47*, 3326–3337, doi:10.1109/TGRS.2009.2022262.

Uttal, T., et al. (2002), Surface heat budget of the Arctic Ocean, *Bull. Amer. Meteorol. Soc.*, *83*, 255–275.

Westwater, E., et al. (2004), The 2004 North Slope of Alaska Arctic Winter Radiometric Experiement, in *Proceedings of the Fourteenth Atmospheric Radiation Measurement (ARM) Science Team Meeting*, U.S. Dep. of Energy, Washington, D. C.

S. A. Clough, Clough Radiation Associates, LLC, 89 Hancock St., Lexington, MA 02173, USA.

J. S. Delamere, E. J. Mlawer, and V. H. Payne, Atmospheric and Environmental Research Inc., 131 Hartwell Avenue, Lexington, MA 02421, USA. (jdelamer@aer.com)

R. R. Gamache, Department of Environmental, Earth and Atmospheric Sciences, University of Massachusetts Lowell, 1 University Ave., Lowell, MA 01854, USA.

D. D. Turner, Space Science and Engineering Center, 1225 W. Dayton St., Madison, WI 53706, USA.